PHYSICS

Origin of the herringbone reconstruction of Au(111) surface at the atomic scale

Pai Li[1] and Feng Ding[1,2]*

The origin of the herringbone reconstruction on Au(111) surface has never been explained properly at the atomic level because the large periodic length (~30 nm) does not allow ab initio simulations of the system and because of the lack of highly accurate empirical force field. We trained a machine learning force field with high accuracy to explore this reconstruction. Our study shows that the lattice deformation in Au deeper layers, which allows the effective relaxation of the densified and anisotropic top layer lattice, is critical for the herringbone reconstruction. The herringbone reconstruction is energetically more favorable than the stripe reconstruction only if the slab thickness exceeds 12 atomic layers. Furthermore, we reveal the high stability of herringbone reconstruction at high temperatures and that a slight strain of about ±0.2% can induce a transition from the herringbone pattern to the stripe pattern, and both agree well with the experimental observations.

INTRODUCTION

The coordination number of atoms on a transition metal surface is lower than that in the bulk, which generally leads to tensile stresses in the pristine metal surface and a tendency for the surface to reconstruct and release tensile stresses (*1*). Although this tendency holds true for all metals, gold is the only one where the close-packed (111) surface reconstructs into a herringbone pattern under ambient conditions. The reconstruction from a pristine Au(111) surface to a herringbone pattern (fig. S1) can be understood by a two-step process: (i) The top layer densifies into a so-called $22 \times \sqrt{3}$ stripe pattern by inserting an extra Au atom into an <110> atomic chain every 22 lattice constants. This densification creates a slight surface corrugation of 0.2 Å on the surface, which is distinguishable by scanning tunneling microscopy (STM) imaging. (ii) The formation of stripe pattern mainly releases the tensile stress in Au top layer along the <110> direction, and, according to continuum elastic theory (*2*), this stripe pattern is not stable and will further reconstruct into a herringbone pattern with periodic stress domains (*3*). Note that dislocations are formed at the elbows of the herringbone pattern during the reconstruction. These elbows are active sites for absorbing heterogeneous metals, such as Ni and Co (*4*).

The Au(111) surface is one of the most used substrates for many applications, such as being used as the template for organic molecular self-assembly (*5*, *6*), the substrate for low-dimensional materials growth (*7*, *8*), especially for the synthesis of carbon nanoribbon (*9*, *10*). It is also an ideal substrate to explore the chemical or physical properties of various molecular or atomic absorbents (*11*–*13*). In previous studies, especially theoretical calculations, the surface reconstruction was generally ignored and, thus, the full understanding of the impact of Au(111) surface reconstruction on these research studies is still an issue.

Theoretically, ab initio methods have been used to study the simple $22 \times \sqrt{3}$ stripe reconstruction using four- to five-layer slab models with about 200 atoms in the primitive cell (*14*–*16*). The herringbone pattern has a much larger period length of ~30 nm (*17*, *18*), which makes it impossible to explore using ab initio methods. Continuum elastic theory revealed the importance of long-range elastic interactions in deeper layers of the herringbone reconstruction, but it lacks atomic details, such as the role of elbow dislocation that cannot be properly considered (*19*). Many atomistic models—such as the two-dimensional (2D) Frenkel-Kontorova (FK) model (*19*, *20*), the tight-binding second-moment approximation (*21*), and the embedded-atom method force field (*22*, *23*)—have been applied to explore the Au(111) surface reconstruction. On the basis of these approaches, defective energy in the elbows, strain distribution, and lattice distortions was discussed. For example, Bulou and Goyhenex (*21*) found that the hydrostatic pressure is greatest in the elbows of the herringbone pattern, which partially explains the fact that Au atoms in the elbows are easily substituted by smaller metal atoms. Unfortunately, all these previous studies showed that herringbone reconstruction from the simple $22 \times \sqrt{3}$ stripe pattern is energetically unfavorable, which resulted in a long-standing puzzle about the origin of the Au(111) herringbone reconstruction at the atomic level. For example, the surface energy of the herringbone superstructure calculated by tight binding is even higher than that of the pristine surface (*21*). The atomic simulation is still a challenge due to the very large supercell size of the herringbone pattern and the subtle energy change during the reconstruction. The former requires high computational efficiency, and the latter requires high accuracy of the interatomic potential. Both empirical potentials and ab initio methods meet only one of the two critical requirements.

In this work, we used the state-of-the-art machine learning method to train an Au machine learning force field (MLFF) for the exploration of the Au(111) surface. Our MLFF-based atomic simulations show that herringbone reconstruction is energetically more favorable than stripe reconstruction. We reveal that large deformations in deeper layers are critical for the herringbone reconstruction, which leads to further relaxation of the atoms in the top layers. In addition, we examine the vibration contribution to the free energy via molecular dynamics (MD) simulations and reveal the high stability of the herringbone reconstruction at elevated temperatures. With the help of our MLFF, we show that a slight strain can induce a transition from herringbone pattern to stripe pattern, in accordance with the reported experimental results.

[1]Center for Multidimensional Carbon Materials, Institute for Basic Science (IBS), Ulsan 44919, Republic of Korea. [2]Department of Materials Science and Engineering, Ulsan National Institute of Science and Technology (UNIST), Ulsan 44919, Republic of Korea. *Corresponding author. Email: f.ding@unist.ac.kr

RESULTS

The Au MLFF was trained using the DeePMD-kit package (*24*). The structures in the training set were labeled with energies and forces calculated using density functional theory (DFT) as implemented in the Vienna Ab initio Simulation Package (VASP) (*25*, *26*). MLFF-MD simulations were realized with large-scale atomic/molecular massively parallel simulator (LAMMPS) (*27*) and atomic simulation environment (ASE) (*28*). We adopted an iterative scheme with a series of training/MLFF-MD/labeling loops (*29*) to generate the complete training set, for which four sets of structures are built (more details can be found in Methods). A total of 11,008 structures were labeled, containing about 3 million force components. One thousand structures were extracted randomly as a test set, and all the others were used to train MLFF. The root mean square error of the final MLFF is very low, 0.85 meV/atom for energy and 11.2 meV/Å for force (Fig. 1, A and B). The calculated phonon dispersion (*30*) and mechanical properties of both Au bulk and surfaces are in agreement with those obtained by using DFT calculations (Fig. 1, C and D, and table S1). As shown in Fig. 1E, the MLFF-MD simulation and structure relaxation lead to a herringbone pattern that perfectly matches the experimental STM pattern. All this indicates the high accuracy of our Au MLFF.

Tensile stress relaxation was considered as the main driving force of the Au(111) reconstruction. On the basis of our MLFF calculations, the pristine Au(111) surface has an isotropic tensile stress of 164.1 meV/Å^2 as shown in Table 1. The formation of the 22 × $\sqrt{3}$ stripe reconstruction reduces the stress along the compressed direction by 42% (to 94.5 meV/Å^2), but along the perpendicular direction, it only reduces by 11% (to 148.4 meV/Å^2). DFT calculation using a five-layer stripe model containing 222 atoms shows very similar tensile stress reduction from 168.5 to 99.6 meV/Å^2 and from 168.5 to 156.2 meV/Å^2, respectively. The herringbone reconstruction lowers the anisotropicity of the surface stress as compared to the stripe one, but the mean value of diagonal stress of the former (121.15 meV/Å^2) is almost the same as the latter (121.45 meV/Å^2). Overall, the herringbone reconstruction reduces the tensile stress by about 26% from that of the pristine Au(111) surface, which is in good agreement with the experimentally reported value of 22% (*32*). Note that neither the herringbone nor stripe reconstruction reduces the surface stress to near zero, which implies that the origin of the herringbone reconstruction cannot be fully understood by a continuum model and that the atomistic details, such as the energy of atomic stacks and dislocations, must be considered.

Atomistic models used in previous studies generally ignored distortion in deeper atomic layers. In 1992, Narasimhan and Vanderbilt (*19*) adopted the FK model with parameters fitted by DFT calculations to explore the Au(111) surface reconstruction. Their FK model, with a rigid truncated substrate, showed that the stripe reconstruction was more stable than the herringbone reconstruction, and the authors concluded that long-range elastic deformations in Au bulk must be considered. However, because of the lack of substrate relaxation in their model, they failed to explain how the herringbone reconstruction is stabilized by long-range elastic deformations.

As shown in Fig. 2, our atomic simulation gives notable distortion in deeper layers. This distortion is generated during the two-step herringbone reconstruction process. First, during the strip reconstruction (Fig. 2B), the densification of the top layer exerts shear forces in the deeper layers, leading to a periodic deformation in the *x* and *y* directions. The corrugated top layer also causes shifts in the *z* direction for atoms in the deeper layers. Second, further reconstruction into the herringbone pattern induces large displacements along the *y* direction in the deeper layers to balance the shear force from the top layer. For the herringbone reconstruction, the distortion of the second layer along the *y* direction has the largest amplitude of ~0.5 Å near the domain walls (Fig. 2A), which is much larger than that of the stripe reconstruction (~0.10 Å) as seen in Fig. 2B. To quantify the deformation decay rate in the deeper layers, we calculated the SD of the atomic displacements in each layer. As shown in Fig. 2C, the displacement along the *x* direction decreases exponentially fast and reaches near zero at ~10th layer; along the *z* direction, the decay is slower and approaches zero at ~20th layer. On the other hand, the displacements along the *y* direction decay very slow, implying a thickness-dependent behavior of the herringbone pattern, which is in stark contrast to that of the stripe reconstruction (Fig. 2D).

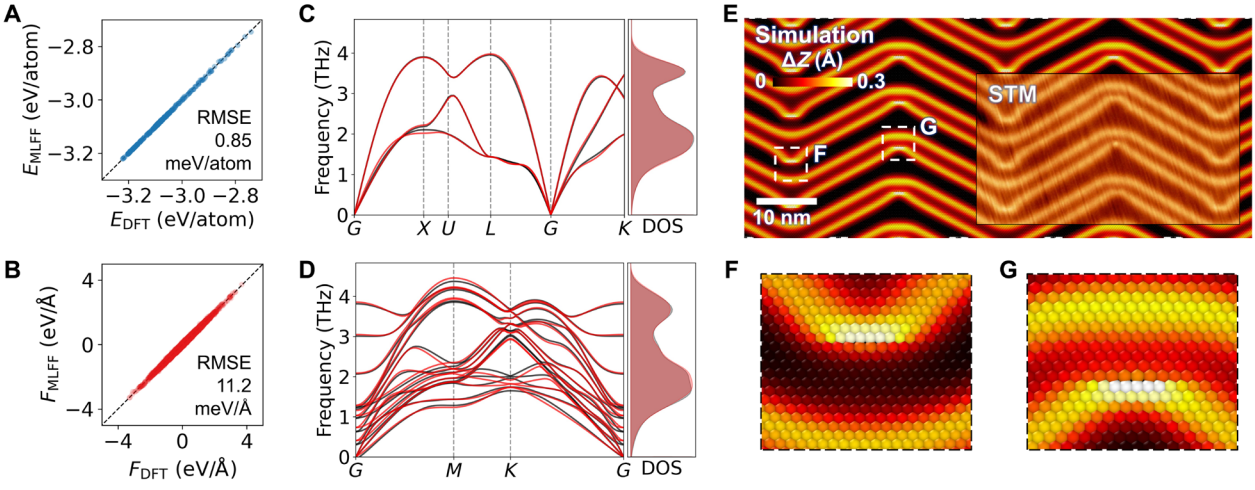

Fig. 1. Performance of the MLFF and the simulated Au(111) surface reconstruction. (**A**) Energy and (**B**) force errors of the MLFF evaluated on a test set of 1000 structures. RMSE, root mean square error. (**C** and **D**) Phonon dispersion and density of state (DOS) for (C) Au bulk and (D) five-layer slab with pristine Au(111) surfaces. DFT and MLFF results are shown in black and red, respectively. (**E**) The simulated Au(111) reconstruction pattern compared to the experimentally observed STM pattern. The STM pattern is adapted from the literature (*31*) with rotation. (**F** and **G**) The atomic details of the two elbows in (E).

Considering the large deformation along the y direction, it is necessary to revisit the original 2D FK model where all the atoms in the deeper layers are frozen at the face-centered cubic (fcc) lattice sites. In such an FK model, all top-layer atoms located on a substrate are modeled with a periodic potential, and all nearest neighboring atoms are connected by a spring force. The system energy is given by (*19*)

$$E = \sum_i V_S(\mathbf{r}_i) + \sum_j k(l_j - b)^2/2 \quad (1)$$

$$V_S(\mathbf{r}) = \sum_{\mathbf{G}} V_S(\mathbf{G})\, e^{-i\mathbf{G}\cdot\mathbf{r}} \quad (2)$$

where i denotes the Au atoms and j denotes the bonds (springs) on the top layer, k is the spring constant, l_j is the length of the jth bond, b is the equilibrium bond length, $\mathbf{G}$ is the reciprocal vector of the lattice, and $V_S(\mathbf{G})$ is the coefficient of the 2D Fourier expansion of the periodic substrate potential. To account for the large elastic deformation along the y direction in the deeper layers, we modified the substrate potential field by introducing a periodic sinusoidal deformation along the y direction

$$V_S(\mathbf{r}) = \sum_{\mathbf{G}} V_S(\mathbf{G})\, e^{-i\mathbf{G}\left[\mathbf{r} - a\cdot\sin\left(\frac{2\pi r_x}{L_x}\right)\cdot\hat{\mathbf{y}}\right]} \quad (3)$$

where a is the y-deformation amplitude, Lx is the periodic length of the herringbone pattern along the x direction, and $\hat{\mathbf{y}}$ is the unit vector along the y direction. The sinusoidal deformation mimics the large deformations in the second layer of the herringbone reconstruction. The substrate potential fields of the FK and MFK models are illustrated in Fig. 3A. This potential field makes those original long Au bonds shorter and those short bonds longer (Fig. 3B), which results in an anisotropic stress relaxation of the top-layer atoms as can be understood via a spring interaction picture (fig. S2).

Within a certain range, a larger deformation in deeper layers releases more stress anisotropy in the top layer as shown in Fig. 3C, but this comes at the expense of an elastic energy penalty in the deeper layers. This elastic energy penalty in the deeper layers can be estimated as a function of deformation amplitude. Without taking into account the deeper layer deformation, the energy in the top layer of the herringbone reconstruction is about 1 eV per supercell greater than that of the strip reconstruction, which is consistent with previous studies (*19*). As shown in Fig. 3C, by taking into account the deformation in the deeper layers, the energy of the top layer decreases rapidly with the increase of the deformation amplitude, a. At the same time, the energy penalty of deeper-layer deformation increases rapidly. The sum of these two terms leads to a total energy minimum at ~0.5 Å deformation amplitude, which is consistent with our MLFF results.

To verify our above conclusions, we build a series of Au slab models with a fixed bottom layer and a thickness ranging from 5 to 32 layers. For the relaxed model with only five layers, the distortion

Table 1. Surface stresses of different Au(111) surfaces. Principal elements of the stress tensor for different surfaces. The pristine Au(111) surface is isotropic. For the stripe reconstruction, the first principal axis is along the soliton line and the second principal axis is perpendicular to the first. For the herringbone reconstruction, the second principal axis is parallel to the domain wall and the first is perpendicular to the domain wall. Values in brackets are obtained by DFT calculations. The unit of surface stress is in millielectron volt per square angstrom.

	First principal	Second principal
Pristine	164.1 (168.5)	164.1 (168.5)
Stripe (5 layers)	149.7 (156.2)	94.1 (99.6)
Stripe (32 layers)	148.4	94.5
Herringbone (32 layers)	133.8	108.5

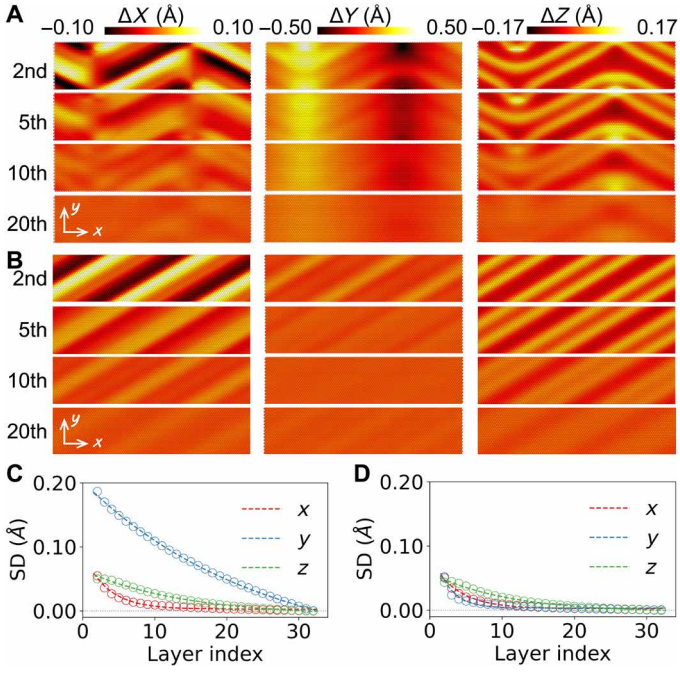

Fig. 2. Deeper layer atomic displacements in reconstructed 32-layer Au(111) slab models. The displacements of Au atoms in the second to 20th atomic layer along the x, y, and z directions in the (**A**) herringbone and (**B**) stripe reconstructed 32-layer models. The SD of the displacement in the x, y, and z directions for each layer in the same (**C**) herringbone and (**D**) stripe reconstructed 32-layer models.

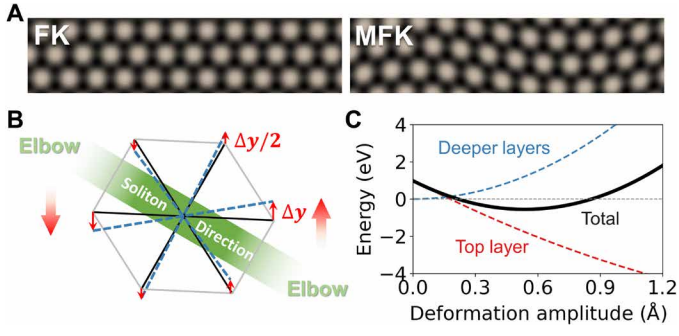

Fig. 3. The new FK model that counts the displacement of the substrate. (**A**) The substrate potential energy surface (PES) in the top view given by the original FK and the modified FK (MFK) models. Brighter color corresponds to higher energy. For the MFK model, a much shorter L_x is adopted for visualization. (**B**) Illustration of the change in the local atomic environment of a top-layer atom due to the deformation of the deeper layers. Six nearest neighbor atoms are located at the vertices of the hexagon (shown in gray) that is uniaxially compressed due to the stripe reconstruction. The small red arrows denote the displacement along the y direction, and the blue dashed lines give the final configuration of the local atomic environment. (**C**) Energy contributions from the top layer (red dashed curve), deeper layers (blue dashed curve), and their summation (black solid curve).

amplitude of the second layer in the *y* direction is only 0.15 Å, and the herringbone reconstruction has higher energy than the stripe reconstruction by ~0.5 eV per supercell (Fig. 4). The herringbone reconstruction prevails over the stripe reconstruction if the layer number is greater than 12. When the model thickness reaches 32 layers, the energy difference is about to converge at around −0.6 eV. This result indicates that a thin slab model is not sufficient to relieve the anisotropic stress in the top layer of the herringbone pattern due to the very small deformation along the *y* direction in the deeper layers. The local energy difference between 5- and 32-layer surfaces is presented in fig. S3. We note that, although gold is a well-known soft metal, the gain in energy due to the herringbone reconstruction is small. For a given deformation, the softer the material, the smaller the energy penalty for deformation in the deeper layers, and thus, the herringbone pattern is more favorable. This analysis also indicates that the fcc(111) herringbone reconstruction is less favorable in hard metals such as platinum, whose shear modulus is more than twice that of gold (*33*), and it does not form a herringbone pattern (*34*, *35*).

The subtle energy difference between the herringbone and stripe pattern makes the herringbone pattern easily affected by some external factors. As reported before, this pattern can be affected by multiple vacancies created by STM tips (*36*), ion sputtering induced vacancy islands (*37*), surface steps (*23*), and species adsorption (*31*). Furthermore, the pristine Au(111) surface has a lower atomic density on the top layer compared to the reconstructed surface and thus has more low-frequency vibrational modes (*38*). It should lower the relative stability of the reconstructed surface at high temperatures due to the vibrational free energy difference. However, STM measurements show that the herringbone pattern exhibits high stability at 400 K (*39*), and the densified surface phase has been observed at 1250 K in x-ray scattering experiments (*18*).

Our high-accuracy MLFF allows us to explore the temperature effects on the stability of the reconstructed surfaces. To account for the temperature-induced vibrational free energy, we performed MLFF-MD simulations to obtain the local vibrational density of state (LVDOS) from the Fourier transform of the velocity autocorrelation function. Our results show that the free energy difference between the pristine and the reconstructed surfaces decreases with the increase of the temperature as shown in Fig. 5A. However, below the Au melting point, the reconstructed surfaces are always more stable than the pristine ones, in accordance with the experimental observations. Note that the increase in temperature also leads to an increase in the free energy difference between the herringbone and stripe reconstructions as shown in Fig. 5B. The difference in phonon DOS between pristine and reconstruction surfaces is notable, but that between stripe and herringbone patterns is not obvious (Fig. 5, C and D). A clear difference is that the LVDOS of the top layer of the herringbone pattern is more isotropic than that of the stripe pattern (fig. S4), which is consistent with the surface stress analysis. The herringbone structure has slightly more LVDOS on the soft-phonon side and less on the hard side, which accounts for their large free energy difference at a higher temperature. We also note that the pristine Au(111) surface corresponds to a local minimum of the potential energy surface (PES), and thus, the transition to the herringbone structure is not phonon-modulated.

The formation of asymmetric herringbone patterns and the transition from herringbone to stripe patterns induced by applied strains have been largely observed (*40*–*42*), but an accurate theoretic analysis is still missing. To study the effect of strain on the Au(111) surface reconstruction, we applied tensile/compressive strain along with one of the soliton directions of the herringbone pattern. As shown in Fig. 6A, the surface pattern is very sensitive to the applied strain. The mirror-symmetric herringbone pattern is stable on a strain-free Au(111) surface only, and a slight strain of 0.1% introduces notable changes in the pattern (Fig. 6B). The grain, with its soliton direction parallel to the strain direction, shrinks/expands if a tensile/compressive strain is applied. When the magnitude of the tensile/compressive strain becomes larger than ~0.2%, the stripe pattern supersedes the herringbone pattern. We note that the strain response is asymmetric. If a stripe pattern along a specific direction is energetically more stable under a tensile strain, then it is less stable under a compressive strain. These results are obtained with relaxed static energy, corresponding to a low-temperature case. After considering the vibrational free energy corrections, the herringbone pattern becomes slightly

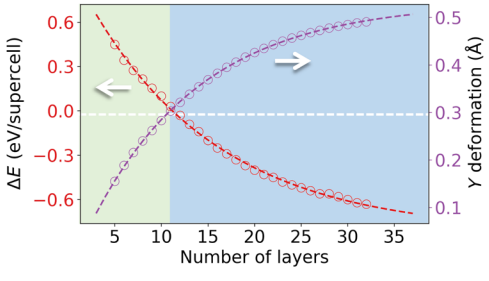

Fig. 4. The comparison of herringbone and stripe reconstructed Au(111) slabs of different thicknesses. The energy difference between herringbone and stripe models (red curve) and the corresponding deformation amplitude of the second layer along the *y* direction (purple curve) for herringbone models with different thicknesses, ranging from 5 to 32 layers. For each model, the bottom layer is fixed in the calculation.

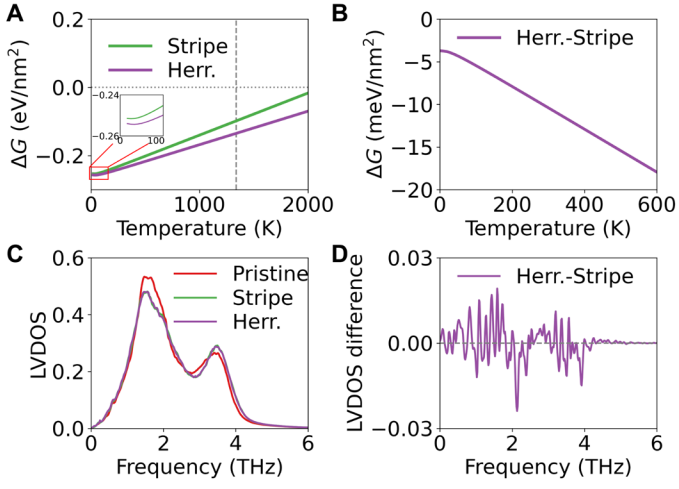

Fig. 5. Temperature-dependent stabilities of pristine, herringbone, and stripe-constructed Au(111) surfaces. (**A**) Free energy difference between the reconstructed surfaces and the pristine Au(111) surface at different temperatures. The vertical dashed line denotes the Au melting point of 1337 K. The inset shows the magnified zone around $T = 0$ K. (**B**) Free energy difference between the herringbone and stripe reconstruction at different temperatures. (**C**) LVDOS of pristine, stripe, and herringbone surfaces including top three layers. (**D**) The LVDOS difference between herringbone and stripe surfaces.

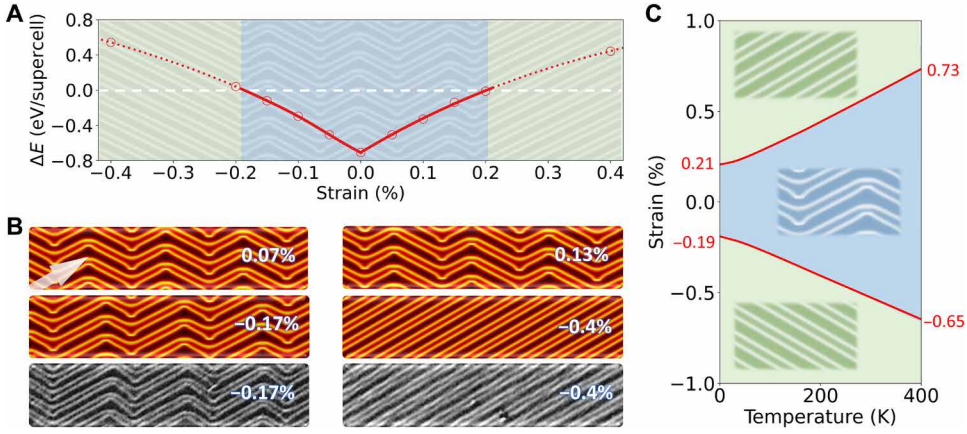

Fig. 6. Au(111) surface reconstruction with the applied strains. (**A**) The energy difference between the herringbone and stripe models under strain. The asymmetric herringbone becomes metastable when the applied strain exceeds about ±0.2%, and the stripe pattern supersedes. (**B**) The corresponding herringbone pattern for different applied strains. The white transparent arrow gives the direction of the applied strain. The gray STM images presented as comparisons are adapted from (*43*). (**C**) Diagram of Au(111) surface reconstruction with respect to temperature and applied strain.

more stable than the stripe pattern and the transition strain shift to about ±0.6% at room temperature (see Fig. 6C). Our trial MD simulations give consistent results (fig. S7). In experiments, the transition strain is estimated to be around 0.5% (*43*), which is in good agreement with our result.

DISCUSSION

The herringbone reconstruction on Au(111) surface is first formed by densification into the stripe pattern and then the transformation into the herringbone pattern. The stripe pattern originates from the uniaxial densification of the pristine Au(111) surface due to the large tensile stress of the latter. For late transition metals (4d and 5d series), the surface tensile stress is mainly aroused by the d-band width shrink due to the reduced coordination number (*1*). We calculated the 5d electron density of states for bulk, Au(111) pristine, and $22 \times \sqrt{3}$ reconstructed surface as shown in fig. S8. The bulk system has the widest d-band, while the pristine surface has the narrowest one. The densified $22 \times \sqrt{3}$ reconstruction slightly recovers the d-band width. This picture is consistent with the fact that the densification releases a small amount of surface stress (~22%) from the pristine surface.

For Au, its d-orbitals are about fully occupied, and thus, we do not expect a very strong d-binding between Au atoms. For others with unoccupied d-orbitals such as Pt, its stronger d-d interaction leads to shorter bond length, larger cohesive energy, and stronger surface stress as compared to Au. Therefore, the driving force for surface atom densification is even larger than that for Au (*44*). However, to densify the surface, a portion of atoms is inevitably pushed onto the bridge or top sites of the second atomic layer. If the direction-dependent d-binding is stronger, bridge or top sites are less stable, and thus, the densification can be suppressed. We calculated the PES of the top-layer atom at different sites. As shown in fig. S9, the energy of a Pt atom locating on a bridge site is about twice that of Au. It implies that the energy penalty of Pt surface reconstruction is much larger than that of Au.

The transformation from the stripe pattern to the herringbone pattern is attributed to the fact that the stripe pattern is more anisotropic and thus mainly allows the stress relaxation along one direction on Au(111). The rearrangement of the stripe pattern into a more isotropic herringbone pattern allows the relaxation of the stress in another direction, which lowers the system energy. However, the introduction of defects, which increases the formation energy, is essential to form such a pattern. Thus, the competition between stress relaxation and defect formation is critical for the formation of herringbone patterns.

To summarize the above discussion, we conclude that Au(111) happens to meet the densification condition and that the herringbone pattern is formed with a small energy gain than that of the stripe pattern. Pt(111) is around the critical point so that it tends to densify into a double line pattern, which is substantially different from the herringbone pattern of Au(111) surface, only at higher temperatures or under Pt vapor conditions (*34*).

In short, we have studied the herringbone reconstruction of Au(111) with an accurate MLFF without fitting any experimental knowledge. Our simulated herringbone pattern looks identical to the experimentally observed STM pattern, and the 26% stress relief of the reconstructed surface is consistent with the experimental results as well. We explain how the deformation in deeper layers leads to the stability of the herringbone reconstruction on Au(111) surface. We further reveal the atomistic mechanisms of many experimental observations, such as the strain-induced asymmetric herringbone pattern and the transition from the herringbone pattern to the stripe pattern and the high stability of the reconstructed surface at high temperatures. Our study extends the application of machine learning interatomic potentials and opens a practicable avenue to study large systems outside the scope of competence for both DFT and traditional empirical force fields.

METHODS

DFT calculation

DFT calculations were carried out with the VASP (*25*, *26*). The general gradient approximation parameterized by Perdew *et al.* (*45*) was adopted as the exchange-correlation functional. The projector augmented wave (*46*) method was used to describe core-valence interaction. A kinetic energy cutoff of 400 eV was used for the plane

wave basis set. The energy convergence threshold was set to 1×10^{-5} eV. For structure optimization, the conjugate gradient method was used until the force on each atom was less than 0.01 eV/Å. The slide is separated from its neighboring images in the periodic condition by a larger than 12-Å vacuum layer. The Monkhorst-Pack method (*47*) was used for *K*-point sampling with spacing less than $0.016 \times 2\pi$ Å^{-1}.

Au MLFF training

We used DeePMD-kit (*24*) to train our MLFF with a radial cutoff of 6.5 Å. The size of the fitting net is 240 × 240 × 240. The whole training set can be classified into four categories. For the first part, we built a bulk model, a perfect pristine Au(111) surface model with five atomic layers, and seven similar Au(111) models with different defects or steps on the top layer. We performed a series of MD simulations for each model at more than 10 temperatures ranging from 3000 to 10 K. Here, an iterative scheme is adopted to repeatedly train coarse MLFF for generating new structures (*29*). In each circle, we run MD with the updated coarse MLFF, extract structures from MLFF-MD trajectories to perform DFT static calculations to enrich the training set, and then retrain a better MLFF with the enlarged training set. About 1953 structures are extracted from these calculations. For the second part, we focus on the layer and shear strain effect. We build 15 models with the number of atomic layers ranging from 6 to 20 and performed MLFF-MD simulation with seven temperatures ranging from 800 to 10 K. A total of 330 structures are extracted from MD trajectories, and DFT static calculations are performed for these structures. Further, random shear strains in the range from −5 to 5% are applied to the same 15 models, and 424 more structures are accordingly obtained with MLFF-MD and DFT static calculations. For the third part, we focus on the stripe reconstruction and possible distortions. We built seven $22 \times \sqrt{3}$ and 22×1 densified surface models with or without point defects, surface steps, and uniaxial strains. For this part, we performed structure optimization and ab initio MD (AIMD) simulation at 300 and 600 K. Here, 2478 structures are extracted from these calculations. For the fourth part, we focus on the effect of atomic density and strain on the top layer. We built 12 models with varying degrees of surface densifications from 8×1 (inserting one extra Au atom in every eight atoms in each <110> atomic chain on the top layer) to 30×1 and performed structure optimization and AIMD. Here, 689 structures are extracted. Besides, different uniaxial and uniform strains ranging from −2% to 2% are applied on these 12 models to perform optimization and AIMD, and 3999 more structures are extracted. Combined with primitive cells, isolated Au, and structures with top-layer atom translation on the *xy* plane, we have 11,008 structures in total, containing 2,962,365 force components. We randomly extracted 1000 structures as the test set, and all others are used to train the final MLFF.

Au(111) herringbone reconstruction modeling

The $22 \times \sqrt{3}$ stripe reconstruction model is first built and optimized. Then, two grains are extended and rotated with different angles to build the herringbone pattern assisted with Atomsk (*48*) and ASE (*28*) packages. The bilaterally symmetrical model has a size of $108 \times 15\sqrt{3}$ and 32 layers, containing 103,824 atoms in total. The top layer has 3384 atoms, with its density 4.44% larger than the bulk layers. The periodic length of the herringbone pattern in our model is 317.4 Å, which is around the typical values observed in experiments (*17*, *18*). The asymmetrical models are built similarly, but a nonorthogonal box is used to satisfy the periodicity and asymmetry requirements. For structure optimizations, we first performed MD simulation at 300 K for 10 ps to overcome possible energy barriers, and then, structure optimization was taken until the force on each atom is less than 0.001 eV/Å to get the final energy. LAMMPS (*27*) is used to perform both MD and structure optimizations with MLFF for large supercell models. For both AIMD and MLFF-MD, if otherwise specifically mentioned, the NVT ensemble is used.

Estimation of the deformation energy for deeper layers

The deformation in deeper layers is estimated as an exponential decay

$$D(i) = D(2) \times e^{\alpha(2-i)}$$

where i is the index of layer, $D(2)$ is the deformation in the second layer, and the parameter α is set to be 0.1 to mimic the decay behavior in the bulk. A verification of this exponential form of decay is provided in the Supplementary Materials. The deformation response force is

$$F = \mu A s / d$$

where μ is the shear modulus, A is the area that applied deformation, s is the deformation amplitude, and d is the space between two domain walls. The energy that is needed to induce this deformation on the substrate is estimated as

$$E = 2 \sum_{i=2} \int_0^{D(i)} F ds$$

which is a quadratic function of $D(2)$ and can be solved numerically. The coefficient 2 denotes the two domains in one supercell.

Vibrational free energy calculation

We first run MD simulation in NPT ensemble for Au bulk system to get the equilibrium lattice constant at 300 K. Then, the box sizes of surface models are adjusted according to this equilibrium lattice constant and used for NVT-MD simulations at the same temperature for 30 ps. The velocities at the last 20 ps are extracted to calculate the velocity autocorrelation function. The LVDOS is finally obtained from the Fourier transform of velocity autocorrelation function as (*49*)

$$g(\omega) = \int_0^{\infty} e^{-i\omega t} \frac{\langle \boldsymbol{v}(t)\, \boldsymbol{v}(0) \rangle}{\langle \boldsymbol{v}(0)\, \boldsymbol{v}(0) \rangle} dt$$

where ω is the vibrational frequency, $\boldsymbol{v}$ is the velocity of Au atoms, and the angle brackets denote the ensemble average. The vibrational free energy is subsequently calculated as (*49*)

$$F = k_B T \int_0^{\infty} \ln\left(2 \sinh \frac{\hbar\omega}{2 k_B T}\right) g(\omega)\, d\omega$$

where k_B is the Boltzmann constant, T is temperature, and $\hbar$ is the reduced Planck constant.

Calculation details of the strain-induced reconstruction pattern transition

Because of the different symmetry of the top layer from the deeper layers, we have no way to obtain the optimal reconstructed pattern

for a given strain using structure optimization. Instead, we build a series of reconstruction models with different symmetries as shown in fig. S5. These models are distinguished by symmetry factors. For each model, we applied a series of uniaxial strains ranging from −1 to 1%. As can be expected, the mirror-symmetric structure with a symmetry factor of 0.5 has the lowest energy when no strain is applied. With the symmetry factor deviating from 0.5, the structure energy increases and can be even higher than that of the stripe reconstruction (red curve in fig. S6). When a strain is applied, the local minimum shifts from the center as shown in fig. S6, which indicates that asymmetric structures supersede the symmetric one. We use spline interpolation to find the minimum energy point.

SUPPLEMENTARY MATERIALS

Supplementary material for this article is available at https://science.org/doi/10.1126/sciadv.abq2900

REFERENCES AND NOTES

1. Y. Shiihara, M. Kohyama, S. Ishibashi, Origin of surface stress on late transition metal surfaces: *Ab initio* local stress and tight-binding model. *Phys. Rev. B.* **87**, 125430 (2013).
2. O. L. Alerhand, D. Vanderbilt, R. D. Meade, J. D. Joannopoulos, Spontaneous formation of stress domains on crystal surfaces. *Phys. Rev. Lett.* **61**, 1973–1976 (1988).
3. J. V. Barth, H. Brune, G. Ertl, R. J. Behm, Scanning tunneling microscopy observations on the reconstructed Au(111) surface: Atomic structure, long-range superstructure, rotational domains, and surface defects. *Phys. Rev. B.* **42**, 9307–9318 (1990).
4. J. A. Meyer, I. D. Baikie, E. Kopatzki, R. J. Behm, Preferential island nucleation at the elbows of the Au(111) herringbone reconstruction through place exchange. *Surf. Sci.* **365**, L647–L651 (1996).
5. Q. Fan, L. Yan, M. W. Tripp, O. Krejčí, S. Dimosthenous, S. R. Kachel, M. Chen, A. S. Foster, U. Koert, P. Liljeroth, J. M. Gottfried, Biphenylene network: A nonbenzenoid carbon allotrope. *Science* **372**, 852–856 (2021).
6. N. A. Wasio, R. C. Quardokus, R. P. Forrest, C. S. Lent, S. A. Corcelli, J. A. Christie, K. W. Henderson, S. A. Kandel, Self-assembly of hydrogen-bonded two-dimensional quasicrystals. *Nature* **507**, 86–89 (2014).
7. P. Yang, S. Zhang, S. Pan, B. Tang, Y. Liang, X. Zhao, Z. Zhang, J. Shi, Y. Huan, Y. Shi, S. J. Pennycook, Z. Ren, G. Zhang, Q. Chen, X. Zou, Z. Liu, Y. Zhang, Epitaxial growth of centimeter-scale single-crystal MoS_2 monolayer on Au(111). *ACS Nano* **14**, 5036–5045 (2020).
8. T. F. Jaramillo, K. P. Jørgensen, J. Bonde, J. H. Nielsen, S. Horch, I. Chorkendorff, Identification of active edge sites for electrochemical H_2 evolution from MoS_2 nanocatalysts. *Science* **317**, 100–102 (2007).
9. J. Cai, P. Ruffieux, R. Jaafar, M. Bieri, T. Braun, S. Blankenburg, M. Muoth, A. P. Seitsonen, M. Saleh, X. Feng, K. Müllen, R. Fasel, Atomically precise bottom-up fabrication of graphene nanoribbons. *Nature* **466**, 470–473 (2010).
10. D. J. Rizzo, G. Veber, J. Jiang, R. McCurdy, T. Cao, C. Bronner, T. Chen, S. G. Louie, F. R. Fischer, M. F. Crommie, Inducing metallicity in graphene nanoribbons via zero-mode superlattices. *Science* **369**, 1597–1603 (2020).
11. T. Komeda, H. Isshiki, J. Liu, Y. F. Zhang, N. Lorente, K. Katoh, B. K. Breedlove, M. Yamashita, Observation and electric current control of a local spin in a single-molecule magnet. *Nat. Commun.* **2**, 217 (2011).
12. A. Zhao, Q. Li, L. Chen, H. Xiang, W. Wang, S. Pan, B. Wang, X. Xiao, J. Yang, J. G. Hou, Q. Zhu, Controlling the Kondo effect of an adsorbed magnetic ion through its chemical bonding. *Science* **309**, 1542–1544 (2005).
13. S. Kawai, A. Benassi, E. Gnecco, H. Söde, R. Pawlak, X. Feng, K. Müllen, D. Passerone, C. A. Pignedoli, P. Ruffieux, R. Fasel, E. Meyer, Superlubricity of graphene nanoribbons on gold surfaces. *Science* **351**, 957–961 (2016).
14. Y. Wang, N. S. Hush, J. R. Reimers, Simulation of the Au(111)–$(22 \times \sqrt{3})$ surface reconstruction. *Phys. Rev. B.* **75**, 233416 (2007).
15. F. Hanke, J. Björk, Structure and local reactivity of the Au(111) surface reconstruction. *Phys. Rev. B.* **87**, 235422 (2013).
16. E. Torres, G. A. Dilabio, A density functional theory study of the reconstruction of gold (111) surfaces. *J. Phys. Chem. C* **118**, 15624–15629 (2014).
17. B. Voigtländer, G. Meyer, N. M. Amer, Epitaxial growth of thin magnetic cobalt films on Au(111) studied by scanning tunneling microscopy. *Phys. Rev. B.* **44**, 10354–10357 (1991).
18. A. R. Sandy, S. G. J. Mochrie, D. M. Zehner, K. G. Huang, D. Gibbs, Structure and phases of the Au(111) surface: X-ray-scattering measurements. *Phys. Rev. B.* **43**, 4667–4687 (1991).
19. S. Narasimhan, D. Vanderbilt, Elastic stress domains and the herringbone reconstruction on Au(111). *Phys. Rev. Lett.* **69**, 1564–1567 (1992).
20. N. Takeuchi, C. T. Chan, K. M. Ho, Au(111): A theoretical study of the surface reconstruction and the surface electronic structure. *Phys. Rev. B.* **43**, 13899–13906 (1991).
21. H. Bulou, C. Goyhenex, Local strain analysis of the herringbone reconstruction of Au(111) through atomistic simulations. *Phys. Rev. B.* **65**, 045407 (2002).
22. T. M. Trimble, R. C. Cammarata, The stability of the low temperature surface reconstruction in Au(111). *Mater. Res. Soc. Symp. Proc.* **648**, P3.22 (2001).
23. D. Chauraud, J. Durinck, M. Drouet, L. Vernisse, J. Bonneville, C. Coupeau, Influence of terrace widths on Au(111) reconstruction. *Phys. Rev. B.* **96**, 045410 (2017).
24. H. Wang, L. Zhang, J. Han, W. E, DeePMD-kit: A deep learning package for many-body potential energy representation and molecular dynamics. *Comput. Phys. Commun.* **228**, 178–184 (2018).
25. G. Kresse, J. Furthmüller, Efficiency of ab-initio total energy calculations for metals and semiconductors using a plane-wave basis set. *Comput. Mater. Sci.* **6**, 15–50 (1996).
26. G. Kresse, J. Furthmüller, Efficient iterative schemes for *ab initio* total-energy calculations using a plane-wave basis set. *Phys. Rev. B.* **54**, 11169–11186 (1996).
27. S. Plimpton, Fast parallel algorithms for short-range molecular dynamics. *J. Comput. Phys.* **117**, 1–19 (1995).
28. A. H. Larsen, J. J. Mortensen, J. Blomqvist, I. E. Castelli, R. Christensen, M. Dułak, J. Friis, M. N. Groves, B. Hammer, C. Hargus, E. D. Hermes, P. C. Jennings, P. B. Jensen, J. Kermode, J. R. Kitchin, E. L. Kolsbjerg, J. Kubal, K. Kaasbjerg, S. Lysgaard, J. B. Maronsson, T. Maxson, T. Olsen, L. Pastewka, A. Peterson, C. Rostgaard, J. Schiøtz, O. Schütt, M. Strange, K. S. Thygesen, T. Vegge, L. Vilhelmsen, M. Walter, Z. Zeng, K. W. Jacobsen, The atomic simulation environment—A Python library for working with atoms. *J. Phys. Condens. Matter* **29**, 273002 (2017).
29. P. Li, X. Zeng, Z. Li, Understanding high-temperature chemical reactions on metal surfaces: A case study on equilibrium concentration and diffusivity of C_xH_y on a Cu(111) surface. *JACS Au.* **2**, 443–452 (2022).
30. D. Alfè, PHON: A program to calculate phonons using the small displacement method. *Comput. Phys. Commun.* **180**, 2622–2633 (2009).
31. H. Walen, D. J. Liu, J. Oh, H. Lim, J. W. Evans, Y. Kim, P. A. Thiel, Self-organization of S adatoms on Au(111): √3R30°rows at low coverage. *J. Chem. Phys.* **143**, 014704 (2015).
32. C. E. Bach, M. Giesen, H. Ibach, T. L. Einstein, Stress relief in reconstruction. *Phys. Rev. Lett.* **78**, 4225–4228 (1997).
33. F. Cardarelli, *Materials Handbook: A Concise Desktop Reference* (Springer International Publishing, 2018).
34. M. Bott, M. Hohage, T. Michely, G. Comsa, Pt(111) reconstruction induced by enhanced Pt gas-phase chemical potential. *Phys. Rev. Lett.* **70**, 1489–1492 (1993).
35. R. Pushpa, S. Narasimhan, Reconstruction of Pt(111) and domain patterns on close-packed metal surfaces. *Phys. Rev. B.* **67**, 205418 (2003).
36. Y. Hasegawa, P. Avouris, Manipulation of the reconstruction of the Au(111) surface with the STM. *Science* **258**, 1763–1765 (1992).
37. V. Repain, J. M. Berroir, S. Rousset, J. Lecoeur, Reconstruction, step edges and self-organization on the Au(111) surface. *Appl. Surf. Sci.* **162–163**, 30–36 (2000).
38. T. S. Rahman, *Surface Thermodynamics and Vibrational Entropy* (Springer International Publishing, 2020).
39. P. Kowalczyk, W. Kozlowski, Z. Klusek, W. Olejniczak, P. K. Datta, STM studies of the reconstructed Au(111) thin-film at elevated temperatures. *Appl. Surf. Sci.* **253**, 4715–4720 (2007).
40. L. Bürgi, H. Brune, K. Kern, Imaging of electron potential landscapes on Au(111). *Phys. Rev. Lett.* **89**, 176801–176804 (2002).
41. C. S. Casari, S. Foglio, F. Siviero, A. Li Bassi, M. Passoni, C. E. Bottani, Direct observation of the basic mechanisms of Pd island nucleation on Au(111). *Phys. Rev. B.* **79**, 195402 (2009).
42. T. Giela, K. Freindl, N. Spiridis, J. Korecki, Au(111) films on W(110) studied by STM and LEED—Uniaxial reconstruction, dislocations and Ag nanostructures. *Appl. Surf. Sci.* **312**, 91–96 (2014).
43. O. Schaff, A. K. Schmid, N. C. Bartelt, J. de la Figuera, R. Q. Hwang, In-situ STM studies of strain-stabilized thin-film dislocation networks under applied stress. *Mater. Sci. Eng. A* **319–321**, 914–918 (2001).
44. Ž. Crljen, P. Lazić, D. Šokčević, R. Brako, Relaxation and reconstruction on (111) surfaces of Au, Pt, and Cu. *Phys. Rev. B.* **68**, 195411 (2003).
45. J. P. Perdew, K. Burke, M. Ernzerhof, Generalized gradient approximation made simple. *Phys. Rev. Lett.* **77**, 3865–3868 (1996).
46. P. E. Blöchl, Projector augmented-wave method. *Phys. Rev. B.* **50**, 17953–17979 (1994).
47. H. J. Monkhorst, J. D. Pack, Special points for Brillouin-zone integrations. *Phys. Rev. B.* **13**, 5188–5192 (1976).

48. P. Hirel, Atomsk: A tool for manipulating and converting atomic data files. *Comput. Phys. Commun.* **197**, 212–219 (2015).
49. P. Korotaev, M. Belov, A. Yanilkin, Reproducibility of vibrational free energy by different methods. *Comput. Mater. Sci.* **150**, 47–53 (2018).

Acknowledgments
Funding: This work was supported by the Institute for Basic Science (IBS-R019-D1) of South Korea and the computational resources from CMCM, IBS. **Author contributions:** Conceptualization: F.D. Methodology: P.L. and F.D. Writing draft: P.L. and F.D. **Competing interests:** The authors declare that they have no competing interests. **Data and materials availability:** All data needed to evaluate the conclusions in the paper are present in the paper and/or the Supplementary Materials.

Submitted 30 March 2022
Accepted 22 August 2022
Published 5 October 2022
10.1126/sciadv.abq2900

ScienceAdvances

Origin of the herringbone reconstruction of Au(111) surface at the atomic scale

Pai LiFeng Ding

Sci. Adv., 8 (40), eabq2900. • DOI: 10.1126/sciadv.abq2900

Science Advances (ISSN) is published by the American Association for the Advancement of Science. 1200 New York Avenue NW, Washington, DC 20005. The title *Science Advances* is a registered trademark of AAAS.